Catalysis oxidation of 1,2-dichloroethane and ethyl acetate over ceria nanocrystals with well-defined crystal planes

Qiguang Dai*, Hao Huang, Yu Zhu, Wei Deng, Shuxing Bai, Xingyi Wang, Guanzhong Lu

Lab for Advanced Materials, Research Institute of Industrial Catalysis, East China University of Science and Technology, Shanghai 200237, PR China

ARTICLE INFO

ABSTRACT

The ceria nanorods, nanocubes and nano-octahedrons exposed crystal planes of (1 1 0)/(1 0 0), (1 0 0) and (1 1 1), respectively, are synthesized via simple hydrothermal method, and characterized by XRD, N_2 adsorption, TEM/HRTEM, Raman, OSC and H_2-TPR. Comparing with nanocubes and nano-octahedrons, the ceria nanorods showed higher surface area, smaller crystallite size, more oxygen vacancies, higher OSC and mobility of oxygen. The catalysis oxidation of DCE and EA was investigated over these ceria exposed well-defined crystal planes for the first time. The results indicated that ceria nanorods showed the highest catalysis activities, followed by nanocubes and nano-octahedrons. Moreover, a possible reaction mechanism for the catalytic oxidation of DCE over the ceria catalyst was proposed.

© 2012 Elsevier B.V. All rights reserved.

1. Introduction

Volatile organic compounds (VOCs) consist of a wide range of relatively low molecular-weight compounds that are emitted from a wide range of industrial processes, such as chemical processing, semiconductor manufacture, polymer synthesis and processing, wastewater treatment, and coating operations. Over 300 chemicals are designated as VOCs by the U. S. Environmental Protection Agency, including varieties of aliphatic hydrocarbons, chlorinated volatile organic compounds (CVOCs) and oxygenated volatile organic compounds (OVOCs). Generally, VOCs are linked to photochemical smog, and stratospheric ozone depletion. In addition, they may have inherent toxicity or carcinogenicity. For these reasons, VOCs are carefully regulated, and a number of processes are used to control the emissions of these compounds. Catalytic oxidation is one of the most widely used techniques, due to the lower operating temperature, high selectivity towards the formation of harmless reaction products, and high catalytic performance for the destruction of low concentrations of pollutants. There are, however, significant challenges to the use of catalytic oxidation for the removal of VOCs, such as catalyst deactivation (especially catalysis oxidation of CVOCs [1–13]), toxic or harmful byproduct formation, and the reaction of a multicomponent VOCs mixture cannot typically be predicted from studies on single components. Therefore, the development of more effective and stable catalysts and the

further understanding for the catalytic oxidation of VOCs are very necessary.

Ceria, a catalytic material, has attracted much attention due to its remarkable redox properties and oxygen storage capability (OSC), especially in CO oxidation, water–gas shift and automobile exhaust treatment. In recent years, CeO_2 catalysts also have attracted special attention in catalytic oxidation of CVOCs [1,4,9–12] and OVOCs [14–16], the results shown that CeO_2 as main active component, catalyst promoter or catalyst support reveals unexpected effects. However, it is notable that most studies were carried on ceria nanoparticles exposing different crystal planes. Numerous theoretical simulations have indicated that different crystal planes of ceria such as (1 1 1), (1 1 0) and (1 0 0) exhibit different properties such as surface stability [17,18], oxygen vacancies formation energy [19,20], and interaction with surface molecules [21]. Moreover, ceria nanocrystals with individual crystal surfaces make it easily and accurately to correlate to the catalytic behavior, which helps to design better ceria catalysts. Therefore, recent studies in CeO_2 systems have focused on the development of simple synthetic approaches toward size/shape-controlled nanostructures (dots, rods, wires and tubes), and the investigation of their size/shape-dependent properties. Hydrothermal method had been proven to be a simple method and widely used. The hydrothermally synthesized ceria nanorods, nanocubes, and nano-octahedrons, exposing crystal planes of (1 1 0)/(1 0 0), (1 0 0), and (1 1 1), respectively, have been demonstrated to show different OSC and catalysis activity (such as CO oxidation, ethanol oxidation, ethanol reforming and water–gas shift) [22–29]. However, little studies are carried in catalysis decomposition/oxidation of CVOCs and other OVOCs.

In the present study, ceria nanorods, nanocubes, and nano-octahedrons nanocrystals exposing different crystal facets are synthesized by a facile hydrothermal method, and characterized by XRD, Raman, TEM/HRTEM, OSC and H_2-TPR. Furthermore, catalysis oxidation of 1, 2-dichloroethane (DCE) and ethyl acetate (EA) over the ceria nanocrystals with different morphologies and crystal surfaces was investigated, and a possible reaction mechanism for the catalytic oxidation of DCE over CeO_2 catalyst was proposed.

2. Experimental

2.1. Catalysts preparation

Single-crystalline CeO_2 nanorods, nanocubes and nano-octahedrons (abbreviate to nanoocta) were prepared by a hydrothermal process as reported previously [23,30]. To obtain nanorods and nanocubes, 3 g of $Ce(NO_3)_3 \cdot 6H_2O$ and 35.396 g (9.177 g for nanocubes) of NaOH were dissolved in 80 mL of deionized water, respectively. Then, these two solutions were mixed and kept stirring for 30 min with the formation of milky slurry. Subsequently, the mixed solution was transferred into a Teflon-lined stainless steel autoclave and then heated at 120 and 180 °C for 48 h and 24 h to get nanorods and nanocubes, respectively. After the hydrothermal treatment, the precipitates were washed with distilled water and ethanol, then dried at 60 °C for 12 h and calcined in air (increases from room temperature to 350 °C at the rate of 1 °C min⁻¹ and maintains for 3 h at 350 °C). For CeO_2 nano-octahedrons, 0.87 g of $Ce(NO_3)_3 \cdot 6H_2O$ and 0.0076 g of Na_3PO_4 were dissolved in 80 mL of distilled water. After being stirred at room temperature for 0.5 h, the mixed solution was transferred into a Teflon-lined stainless steel autoclave and heated at 170 °C for 10 h. After being cooled to room temperature, the precipitates were washed with distilled water and ethanol, then dried at 60 °C for 12 h and calcined in air (increases from room temperature to 350 °C at the rate of 1 °C min⁻¹ and maintains for 3 h at 350 °C). The more detailed preparation conditions were presented in Figs. S1–S5.

2.2. Catalysts characterization

2.2.1. Powder X-ray diffraction

The powder X-ray diffraction patterns (XRD) of the samples were recorded on a Rigaku D/Max-rC powder diffractometer using Cu Kα radiation (40 kV and 100 mA). The diffractograms were recorded in the 2θ range of 10–80° with a 2θ step size of 0.01° and a step time of 10 s.

2.2.2. Nitrogen adsorption/desorption

The nitrogen adsorption and desorption isotherms were measured at 77 K on an ASAP 2400 system in static measurement mode. The samples were outgassed at 160 °C for 4 h before the measurement. The specific surface area was calculated using the BET model.

2.2.3. Transmission electron microscopy

High-resolution transmission electron microscopic (HRTEM) images of the synthesized ceria were taken on a JEOL-2010 field emission transmission electron microscope that operated at 200 kV. The TEM images of the powder samples were recorded on a HITACHI H-800 instrument operated at 200 kV.

2.2.4. Raman spectroscopy

The Raman spectra were obtained on a Renishaw in Viat + Reflex spectrometer equipped with a CCD detector at ambient temperature and moisture-free conditions. The emission line at 514.5 nm from an Ar⁺ ion laser (Spectra Physics) was focused, analyzing spot

about 1 mm, on the sample under the microscope. The power of the incident beam on the sample was 3 mW. Time of acquisition was varied according to the intensity of the Raman scattering. The wave numbers obtained from spectra were accurate to within 2 cm⁻¹.

2.2.5. Temperature programmed reduction

H_2-temperature programmed reduction (H_2-TPR) of CeO_2 samples (100 mg) placed at the bottom of the U-shaped quartz tube was investigated by heating CeO_2 samples in H_2 (5 vol.%)/Ar flow (30 mL min⁻¹) at a heating rate of 10 °C min⁻¹ from 50 to 600 °C. The hydrogen consumption was monitored by thermo-conductivity detector (TCD). After the first H_2-TPR analysis, the samples were cooled to 350 °C in Ar flow and re-oxidized for 30 min in O_2 flow at 350 °C, and then the second H_2-TPR analysis was carried out according to the above conditions, and so on.

2.2.6. Oxygen storage capacity measurements

The Oxygen storage capacity (OSC) of the samples was measured at 525 °C under atmospheric pressure in a fixed bed flow microreactor. Then 100 mg of the sample powder was diluted with 100 mg of quartz sand (40–60 mesh) and placed in a U-shaped quartz tube. After the sample was oxidized at 525 °C in O_2 flow for 5 min, and flushed with pure Ar to remove O_2 contamination, H_2 (5.0% in Ar) was pulsed into the reactor and the sample was fully reduced at 525 °C by several times pulses at intervals of 1 min. Afterward, O_2 pulses were introduced at the same temperature to complete the reduction–oxidation cycle of the samples. The H_2–OSC values were determined by the amount of H_2 consumed during the H_2 pulses analyzed by on-line gas chromatography using a thermal conductivity detector.

2.3. Catalytic activity measurement

Catalytic oxidation reactions were carried out in a continuous flow microreactor constituted of a U-shaped quartz tube of 3 mm of inner diameter at atmospheric pressure. 200 mg catalyst was placed at the bottom of the U-shaped micro-reactor. The feed flow through the reactor was set at 40 cm³ min⁻¹ and the gas hourly space velocity (GHSV) was maintained at 15,000 h⁻¹. Feed stream to the reactor was prepared by delivering liquid DCE (EA or the mixture of EA and DCE) with a syringe pump into dry air, which was metered by a mass flow controller. The injection point was electrically heated to ensure complete evaporation of the liquid reaction feeds. The concentration of DCE in the reaction feeds was set at 275 ppm (The concentration of EA was set at 1000 ppm). The temperature of the reactor was measured with a thermocouple located just at the bottom of the microreactor. The effluent gases were analyzed by an on-line gas chromatograph equipped with a FID detector. Mass spectrum was used for the determination of the main intermediates and by-products.

The temperature-programmed surface reaction (TPSR) measurement was carried out under the catalytic activity tests condition in order to detect the evolutions of the reactant and the products. First, the air flow containing a certain concentration of DCE (EA or the mixture of EA and DCE) flowed continuously the catalysts at 80 °C. After the adsorption–desorption reached equilibrium, the catalysts were heated from 80 to 350 °C within 40 min. The reactant and the products were analyzed on-line over a mass spectrometer apparatus (HIDEN QIC-20).

3. Results and discussion

3.1. XRD, BET and TEM analysis of ceria nanocrystals

Fig. 1 shows the XRD patterns of the three ceria samples. The CeO_2 nanorod, nanocube and nanoocta are of pure cubic
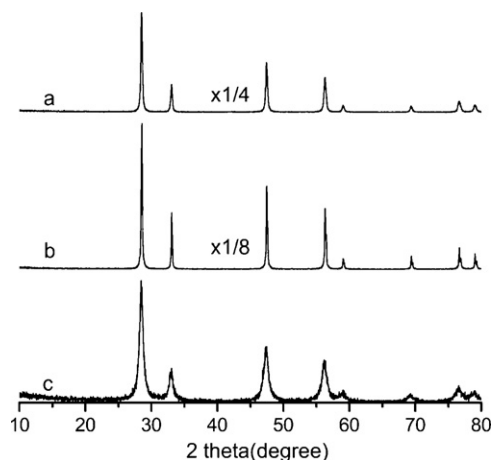
Fig. 1. XRD patterns of as-synthesized ceria nanoocta (a), nanocube (b), and nanorod (c).

phase (fluorite structure, JCPDS 34-0394, space group Fm-3m). The nanocube and nanoocta exhibit relatively higher crystallinity than the nanorod, and the crystallite size, determined from the Scherrer equation, is 16.4 nm for nanorod, 31.2 nm for nanocube, and 25.5 nm for nanoocta. The BET areas of the nanorod, nanocube, and nanoocta are 56, 21, and 10 m^2/g, respectively.

Fig. 2 shows the TEM images of the ceria samples, and is in good accord with reported studies of ceria nanomaterials [22,23,30]. The nanoocta (Fig. 2a, d) is very uniform in size distribution (110–120 nm) and shaped and are dominated by a truncated octahedral shape enclosed by the (1 1 1) facets. The nanocube (Fig. 2b, e) shows less uniform size distribution ranging from 15 to 25 nm, but all in perfect cubic shape, exposing the (1 0 0) surface. The nanorod (Fig. 2c, f) is about 10 nm across and 50–250 nm long. According to previous studies [22,23,30], the synthesized rods grow along the (1 1 0) direction and prefer to expose (1 1 0) and (1 0 0) surfaces. The selected area electron diffraction (SAED) confirmed that the as-obtained CeO$_2$ nanorod, nanocube and nanoocta are of single-crystalline nature (see Fig. S6).

3.2. Raman spectra

Raman spectra of ceria nanorod, nanocube, and nanoocta are presented in Fig. 3. The Raman spectra of all samples show a strong peak at about 460 cm^{-1}, which is attributed to the Raman-active vibrational mode (F$_{2g}$) of fluorite-type structure. It can be viewed as a symmetrical stretching vibration of the oxygen atoms around cerium ions [31]. Furthermore, the Raman spectra also exhibit another three weak bands at around 255, 600 and 1190 cm^{-1}, which are attributed to the doubly degenerate TO mode, the nondegenerate LO mode and the combination of A$_{1g}$, E$_g$ and F$_{2g}$ modes, respectively [32,33]. The broad band at around 600 cm^{-1}, which has been related to the presence of oxygen vacancies due to the presence of Ce^{3+} ions in CeO$_2$ lattice [34] and the ratio of integral intensity of the band of oxygen vacancies and of the F$_{2g}$ mode of fluorite-type structure (A$_{600}$/A$_{460}$) reflects the relative oxygen vacancy concentration. This ratio increases in the following order: nanoocta < nanocube < nanorod, indicating that the amount of oxygen vacancies of as-synthesized CeO$_2$ varies as nanorod > nanocube > nanoocta. Wu et al. [35] also reported that CeO$_2$ nanorod have the most abundant intrinsic defect sites, followed by nanocube and nanoocta.

Additionally, the changes of the Raman mode position and shape in nanomaterials are usually studied using the phonon confinement model (PCM) [36,37]. The evolution of the F$_{2g}$ Raman mode (the mode frequency shift and broadening) strongly depends on

the confinement and inhomogeneous strain effects due to the particle size distribution. With decreasing size, the Raman line shifts to lower energy becoming more asymmetric because of the contribution of interior phonons from the entire Brillouin zone ($q \neq 0$). Therefore, from the Fig. 3, it can be found that the mean particle sizes of ceria nanorod, nanocube, and nanoocta in turn increase, which is consistent with the TEM results.

3.3. OSC and H$_2$-TPR

The oxygen storage capacity (OSC) and redox properties of the samples employed in this work were investigated by O$_2$–H$_2$ titration methods, and H$_2$-TPR. The OSC and H$_2$-TPR profiles of samples are illustrated in Fig. 4(left) and Fig. 4(right), respectively. It can be observed that the OSC of the samples at 525 °C showed significant differences. The CeO$_2$ nanorod exhibited an OSC of 515 μmol H$_2$/g, which is much higher than that of CeO$_2$ nanocube and nanoocta (the value is about 30 and 5 μmol H$_2$/g, respectively), due to easier formation of oxygen vacancies on (1 1 0) and (1 0 0) than on (1 1 1) [38], larger surface area [39] and smaller crystallite size. It is noteworthy that the OSC of CeO$_2$ nanocube is obvious difference with the value reported in the literature [23,40], which is probable that the CeO$_2$ nanocube synthesized in the paper are of larger crystallite size. Additionally, in the five consecutive cycles of the O$_2$–H$_2$ titration, the H$_2$ consumption of the CeO$_2$ nanorod was similar, for the CeO$_2$ nanocube, the OSC maintains stable after two cycles, but the OSC of nanoocta decreases continuously with the O$_2$–H$_2$ titration. This suggests that the CeO$_2$ nanorod is of more reversible redox behavior.

The H$_2$-TPR profiles show that three ceria samples exhibit a single reduction peak at 350–600 °C (Fig. 4 (right, inlet)), and the peak temperature of ceria nanorod is the lowest, followed by nanocube and nanoocta, is about 520, 540 and 585 °C, respectively. However, the H$_2$-consumption (peak area) increases with nanocube, nanoocta and nanorod. Moreover, it can be found that all samples shown an additional shoulder peak about 400–450 °C after the first H$_2$-TPR, and the CeO$_2$ nanorods and nanocubes displayed a new reduction peak at 200–250 °C, which possibly results from the high temperature treatment. Simultaneously, the multiple H$_2$-TPR profiles also show that the CeO$_2$ nanorod is of higher stability. According to the results of OSC and TPR, we suggested that the nanorod should have much higher catalysis activity for the catalysis oxidation of VOCs than the nanocube and nanoocta.

3.4. Catalysis combustion of EA over ceria nanocrystals

Fig. 5 compares the EA conversions over CeO$_2$ nanorod, nanocube and nanoocta. Among all of samples, the CeO$_2$ nanorods sample show the highest activity for the EA catalytic combustion, EA is completely oxidized below 250 °C, and carbon dioxide and water are the main final products. Additionally, a small amount of by-products such as ethanol is formed, without carbon monoxide. However, for the CeO$_2$ nanoocta, the complete oxidation of EA was not achieved even at 350 °C. Additionally, at high GHSV (37,500 h^{-1}), the main product is carbon monoxide over the CeO$_2$ nanoocta, which is possibly related with the low oxygen vacancies, oxygen mobility and redox properties. Seen from the above results, the morphology (crystal plane) of CeO$_2$ nanocrystals has a significant effect on the EA total oxidization, which indicates that the surface activity of (1 0 0) and (1 1 0) is greater than for (1 1 1) planes of CeO$_2$ nanocrystals. The previously reported results [41] indicated that (1 1 1) surface is the most stable and (1 0 0) is the least stable among the low-index surfaces of CeO$_2$. The (1 1 0) surface has been found to be metastable and the surface oxygen vacancies are more stable compared to the (1 1 1) surface.
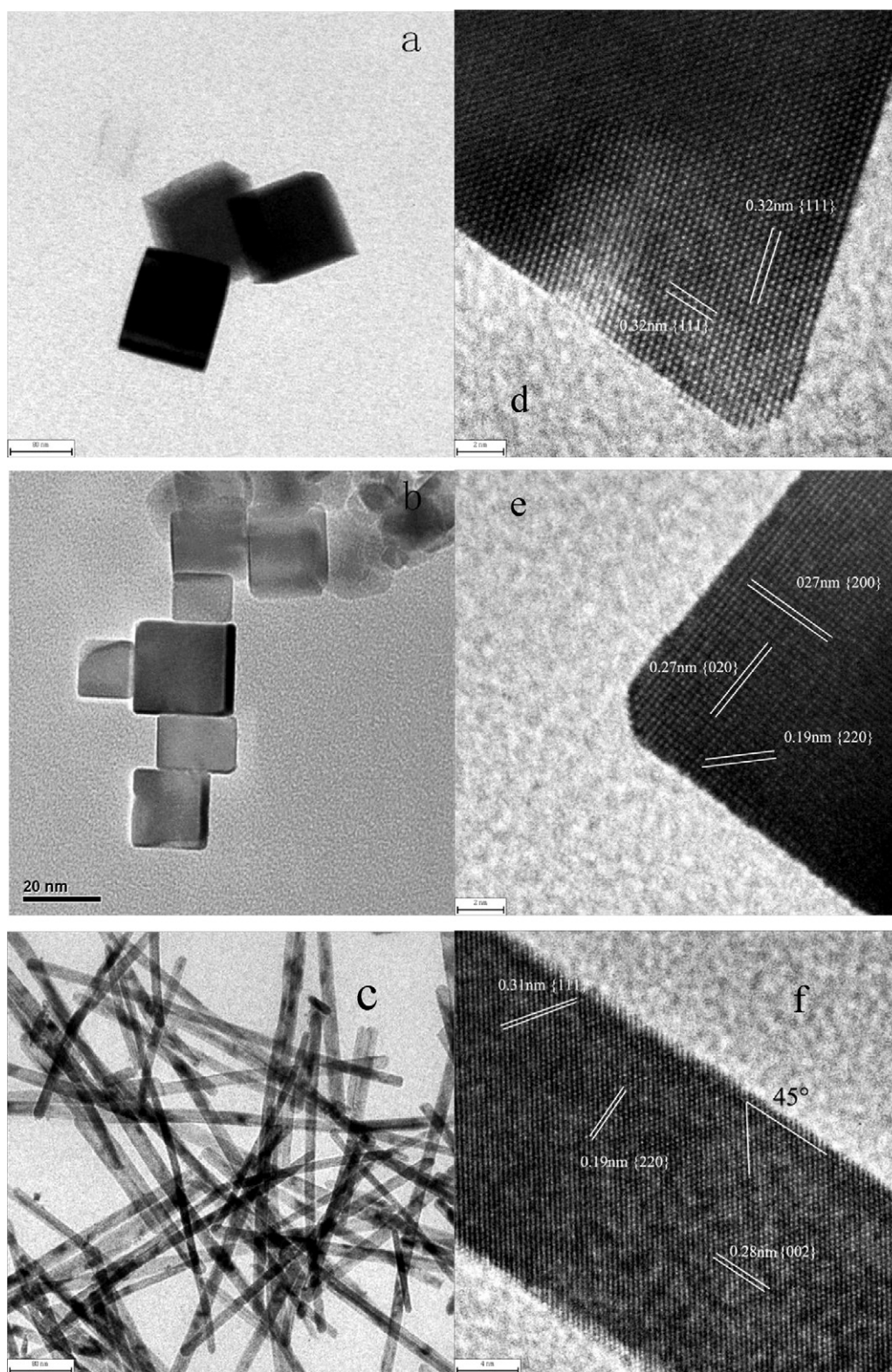
Fig. 2. TEM and HRTEM images of as-synthesized ceria nanorod (a, d), nanocube (b, e), and nanoocta (c, f).

Theoretical studies [42–44] have shown that (1 1 1) is the least active surface, followed by (1 1 0) and (1 0 0). According to the above conclusions, the CeO$_2$ nanocube with (1 0 0) crystal planes should show the highest activity for EA oxidation. However, the results of activity evaluation showed that nanorod was more active than nanocube. This indicates that, besides the reactivity of crystal planes, there are other factors such as crystallite size and surface area for influencing the ceria activity [45] and the concentration of oxygen vacancies may be another main factor.
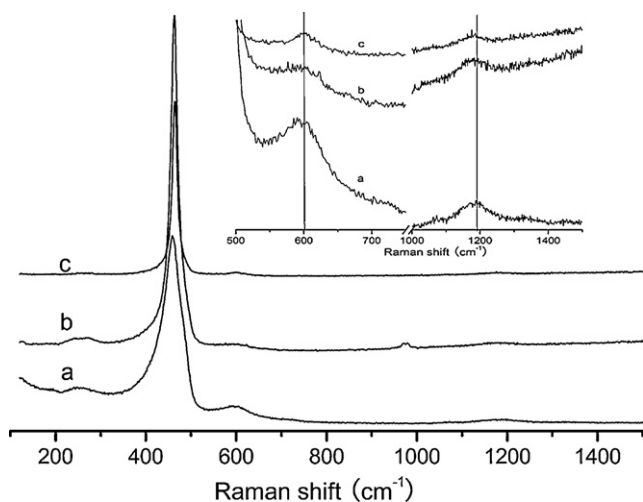
Fig. 3. Raman spectra of ceria nanorod (a), nanocube (b), and nanoocta (c).
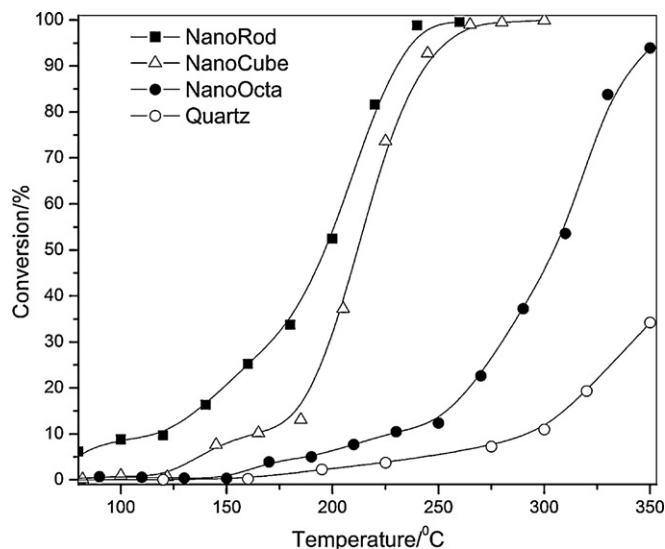

Fig. 5. The light-off curves of EA catalytic combustion over CeO$_2$ nanorod, nanocube and nanoocta. EA: 1500 ppm, GHSV: 15,000 h^{-1}, Catalyst: 200 mg.

3.5. Catalysis decomposition of DCE over ceria nanocrystals

The light-off curves of DCE catalytic decomposition over CeO$_2$ nanorod, nanocube and nanoocta are presented in Fig. 6. Similar with EA catalytic combustion, CeO$_2$ nanorod still show the highest catalysis activity, especially at low temperature region (from 100 to 200 °C). During the decomposition of DCE over all of samples, the

C$_2$H$_3$Cl is only chlorinated organic by-product and the maximum concentration is lower than 10 ppm. It is generally acknowledged [46] that, the first step in the catalytic decomposition of CVOCs is the splitting of first Cl atom, so the ability adsorbing and dissociating the C–Cl bond directly determines the catalytic activities of
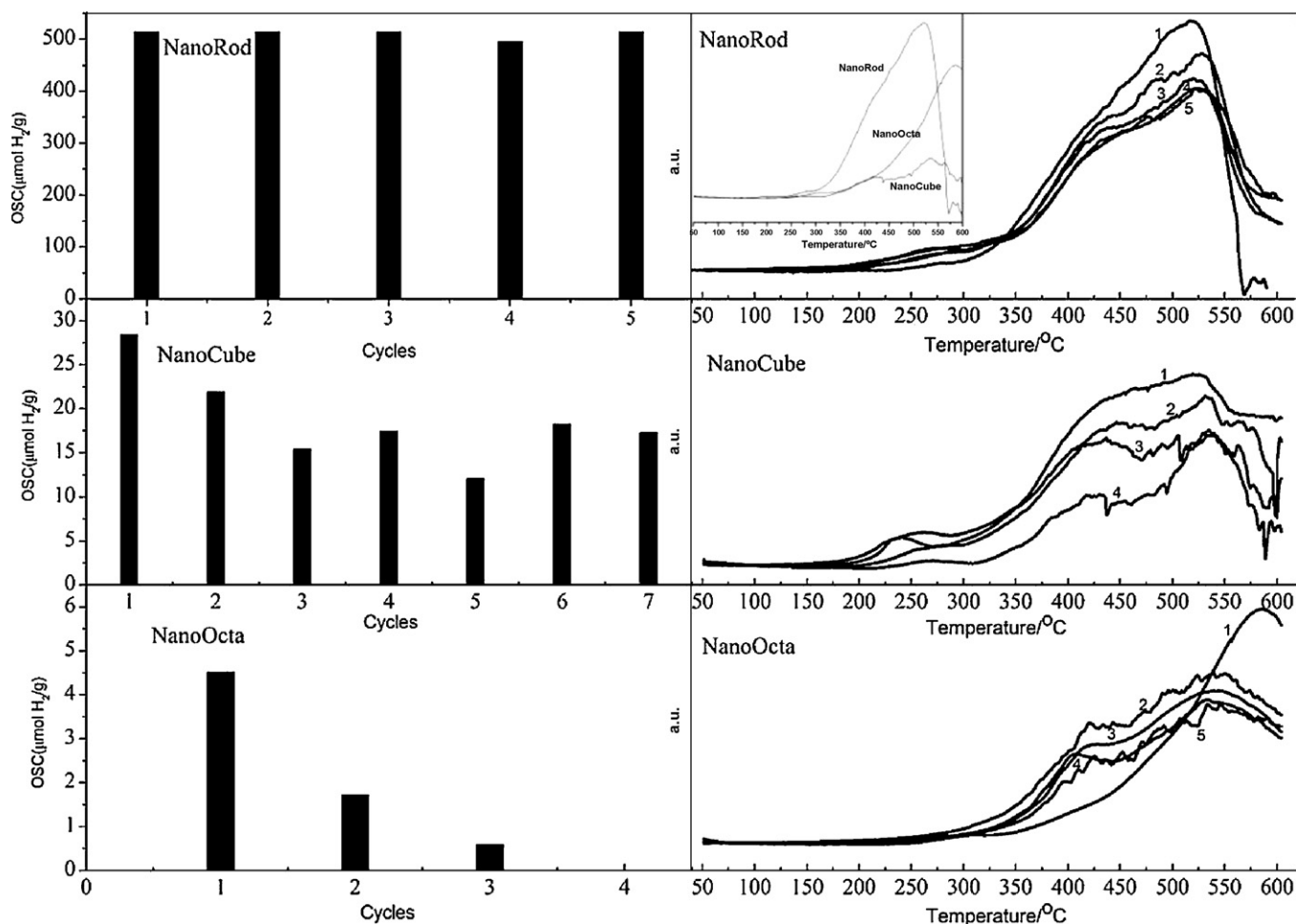

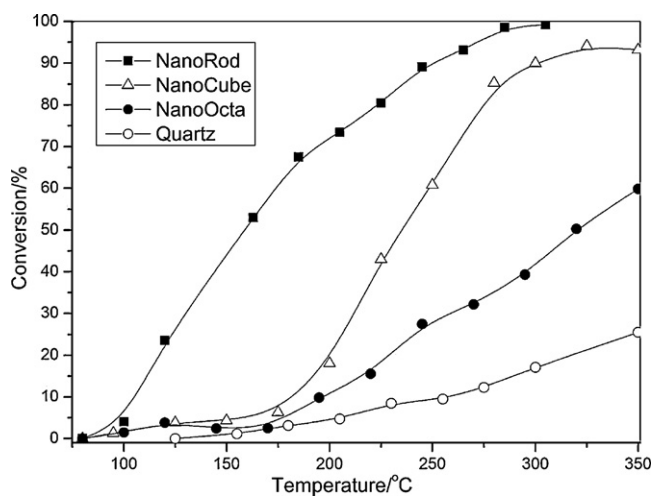Fig. 4. OSC and H$_2$-TPR profiles of ceria nanorod, nanocube and nanoocta.

Fig. 6. The light-off curves of DCE catalytic decomposition over CeO₂ nanorod, nanocube and nanoocta. DCE: 275 ppm, GHSV: 15,000 h⁻¹, Catalyst: 200 mg.

catalysts. Theoretical calculation studies shown that CeO₂ (1 0 0) is of the highest surface energies among CeO₂ (1 1 1), (1 1 0) and (1 0 0), and CeO₂ (1 1 1) have the lowest energy, which implies that the (1 1 0) and (1 0 0) surfaces are less stable than the (1 1 1) surface. The CeO₂ (1 1 1) surface is the most stable, it is also inherently less reactive as compared with the (less stable) CeO₂ (1 1 0) and (1 0 0) [42,47]. Thus, it can be speculated that DCE molecules can be more easily adsorbed and dissociated by CeO₂ (1 1 0) and (1 0 0) than (1 1 1), which results in the CeO₂ nanorod and nanocube possessing higher catalytic activity for DCE catalysis decomposition. The TPSR experiments show that larger amount of DCE desorbed from CeO₂ nanorods at low temperature (<140 °C) than that on nanocubes and nanoocta. Additionally, the incompletely oxidized product, carbon monoxide, is not observed over the three ceria nanocrystals catalysts. Moreover, DCE can be oxidized to CO₂ at absence of gaseous oxygen (in Ar flow, see Fig. S7).

3.6. Mechanism of EA and DCE catalysis oxidation over ceria nanocrystals

In order to further understand the catalytic behavior of the EA and DCE oxidation over CeO₂ catalysts, a series of experiments are carried out over the CeO₂ nanorods and the results are presented in Figs. 7, 8 and 10.

Fig. 7. shown the light-off and stability curves of the binary mixture (the concentration of DCE and EA is 275 ppm and 1500 ppm, respectively) catalytic oxidation over CeO₂ nanorods. As shown in Fig. 7 (upper), DCE conversion is suppressed slightly by EA in a binary mixture. However, EA conversion was almost not affected by the presence of DCE. The reason might be that adsorption of the two reactants occurs on different sites of CeO₂ nanorods (such as Ce^{3+}/Ce^{4+} and oxygen vacancies). The stability tests (Fig. 7(below)) demonstrates that the conversion of EA varied insignificantly in decreasing at 275 °C after 260 min (additional experiments indicate that the deactivation of CeO₂ nanorods for EA catalytic combustion is not observed in the longer stability tests, in the presence of DCE or without DCE). In contrast, the conversion of DCE altered significantly from the initial value 90% to 0% after 260 min. Additionally, in the course of the catalysis activity for DCE decreased, the concentration of by-product ethanol gradually decreased until stabilized at around 10 ppm after complete deactivation for DCE. These results indicate clearly that the catalysis oxidization of DCE and EA over CeO₂ is carried on different active sites. It is speculated that DCE molecule is firstly adsorbed and dissociated on the Ce^{3+} or Ce^{4+}, and then the dissociated DCE is completely oxidized by active oxygen species such as adsorbed oxygen or the migrated lattice oxygen via oxygen vacancies. However, for EA catalysis combustion, oxygen vacancies are the main active adsorption sites. Most of Cl species from DCE decomposition adsorb on the Ce^{3+} or Ce^{4+}, so the conversion of EA over CeO₂ catalysts adsorbed by Cl species were almost unchanged.

Fig. 8 showed the light-off curves and by-product of EA catalytic combustion over the deactivated CeO₂ nanorods for DCE catalysis decomposition. It can be seen that the catalyst completely deactivated by higher concentration of DCE (1000 ppm) at higher temperature (350 °C), the TPSR results are presented in
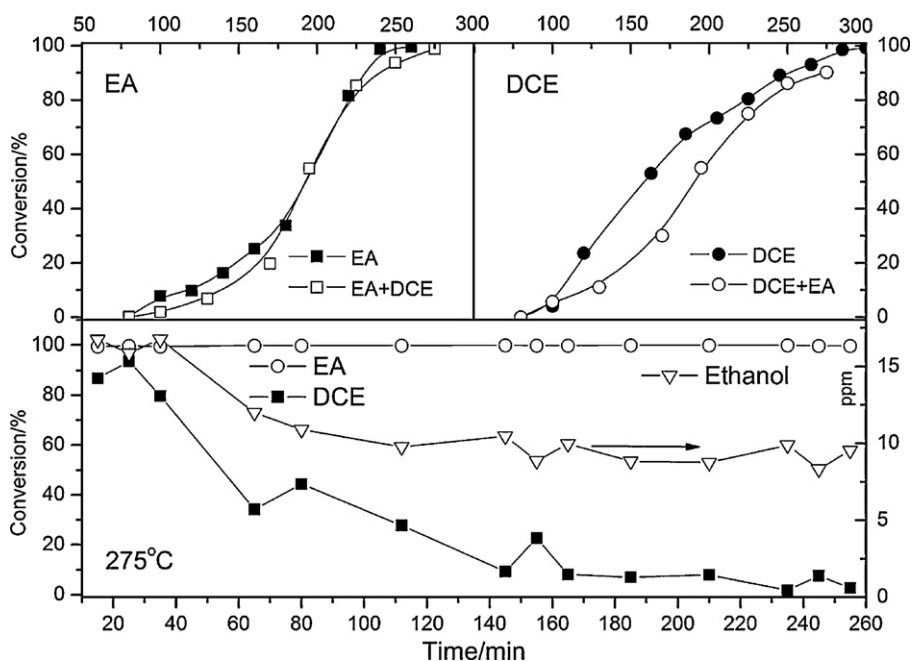

Fig. 7. The light-off and stability curves of the binary mixture catalytic combustion over CeO₂ nanorod. The concentration of DCE and EA is 275 ppm and 1500 ppm, respectively; GHSV: 15,000 h⁻¹; Catalysts: 200 mg.
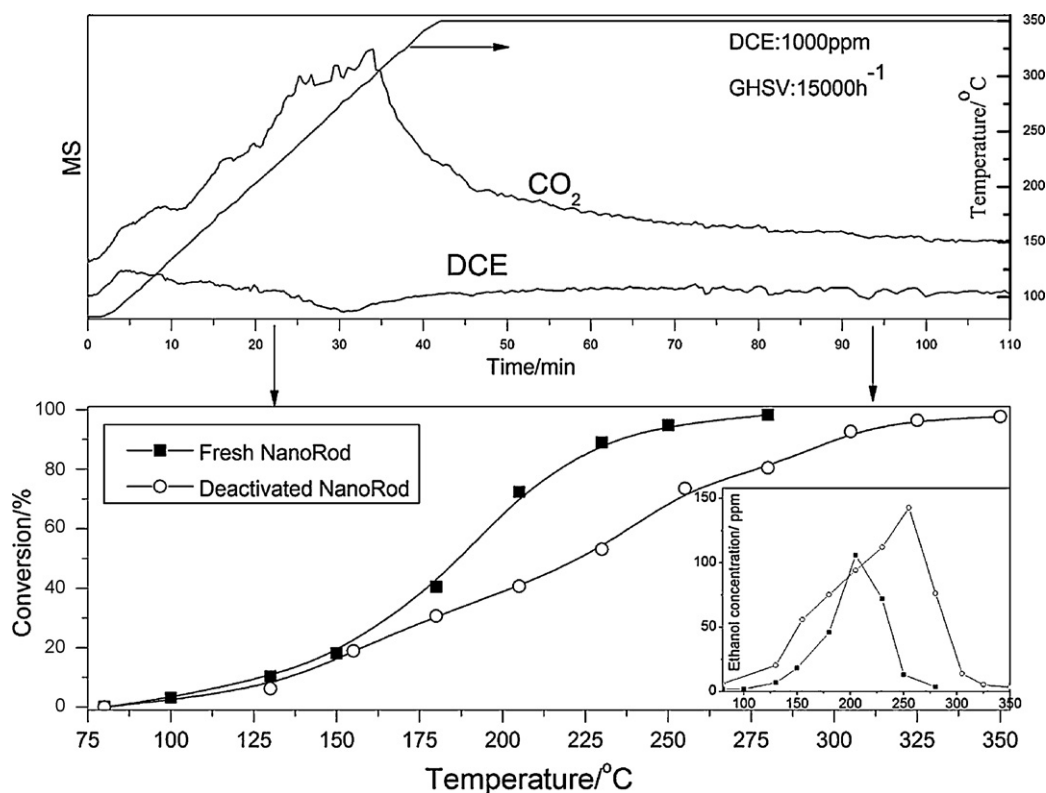
Fig. 8. The light-off curves and by-product of EA catalytic combustion over the deactivated CeO_2 nanorod for DCE catalysis decomposition. The concentration of DCE and EA is 1000 ppm and 1500 ppm, respectively; GHSV: 15,000 h^{-1}; Catalysts: 200 mg.

Fig. 8(upper), still showed very high activity for the EA catalysis combustion but decrease obviously. Moreover, the concentration of by-product ethanol increase compared with that over the fresh catalysts (see Fig. 8 (inset)) and the temperature at which the maximum concentration of ethanol is achieved shifts to higher temperature range. Fig. 9 showed the H_2-TPR profiles of the completely deactivated catalysts by Cl. As shown in Fig. 9, peak temperature of the deactivated CeO_2 nanorods shifts significantly to higher temperature and the peak area (H_2 consumption) is decreased, which indicates that the redox performance of the deactivated catalyst was decreased. Soria et al. [48] investigated the influence of chloride ions on the surface properties of CeO_2

with EPR spectrum. Results on HCl-impregnated CeO_2 showed the generation of different Ce^{4+}–O^{2-} species at chloride-free and chloride-influenced sites of the ceria surface, and the g shift to higher values reveals the influence of chloride ions on the oxygen adsorption centers, which results in higher resistance to reoxidation of these centers. According to the above results, it can be concluded that a large amount of Cl adsorbed on CeO_2 surface inhibits the catalysis activity for EA catalysis combustion, which possibly results from the decrease of redox performance (such as the decrease of oxygen vacancies or migration of lattice oxygen) of the deactivated catalyst.

Fig. 10 presented light-off curves of DCE catalysis decomposition over CeO_2 nanorods, whose are treated with 1500 ppm EA at 350 °C for 75 min (see Fig. 10 (upper)). The results show that the treatment of EA does not affect the activity of CeO_2 nanorods for DCE catalysis decomposition. However, the previous results (Fig. 7) showed that the presence of EA suppressed slightly DCE conversion in a binary mixture. Therefore, it is proposed that oxygen vacancies (or active oxygen species) are common active sites of EA and DCE catalysis combustion over CeO_2.

Based on the above experiments, characterizations and the previous results [1,2], a plausible reaction mechanism can be proposed for the catalytic combustion of DCE and EA over CeO_2 catalysts (Scheme 1).

Firstly, the Cl of DCE adsorbs on the Ce^{3+} sites, and the dissociating and splitting of C–Cl bonds occurs simultaneously. However, for the EA, the oxygen-defect sites would be the active centers, and the EA molecules are activated by oxygen vacancies. The next step is oxidation of the dissociated and activated DCE (and EA). The DCE and EA oxidation follows a Mars–van Krevelen mechanism that necessitates the participation of the lattice oxygen in the CeO_2 catalyst. The dissociated DCE and EA molecules on different active sites is initially oxidized by oxygen from the bulk to the surface via a vacancy hopping mechanism [49], and the partially reduced CeO_{2-x}
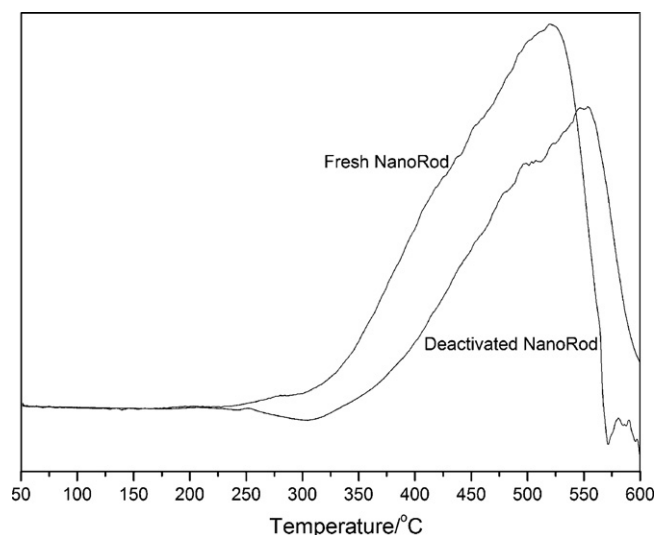

Fig. 9. The H_2-TPR profiles of fresh and completely deactivated CeO_2 nanorod.
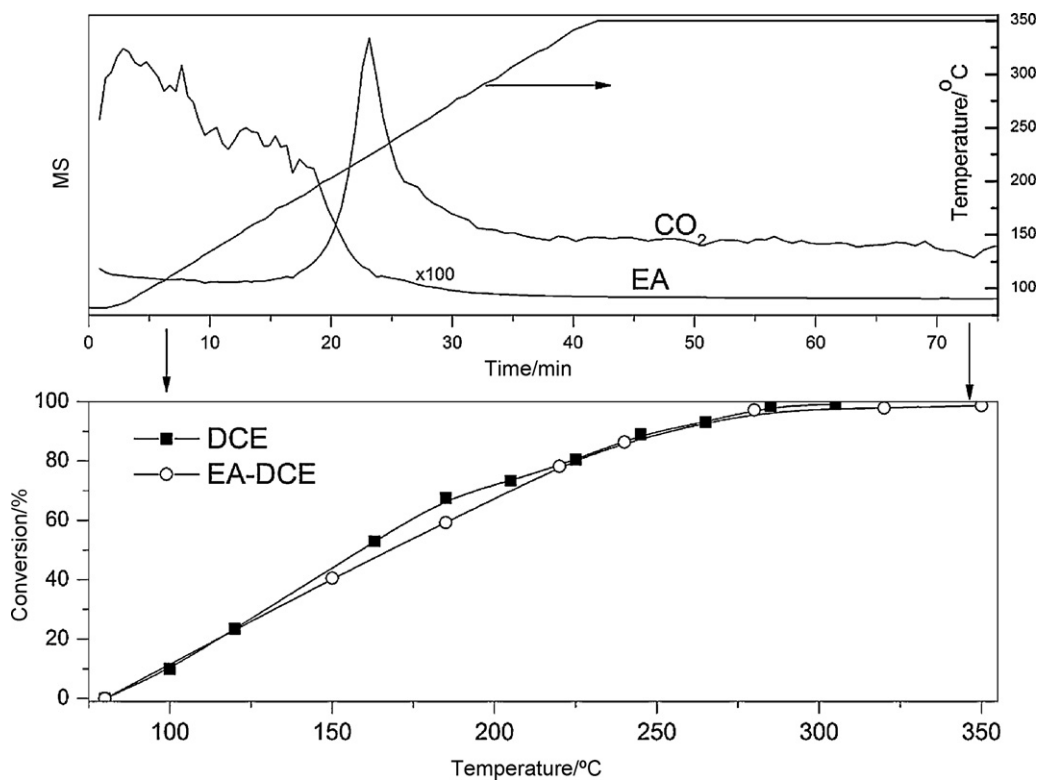
Fig. 10. The light-off curves of DCE catalysis decomposition over CeO_2 nanorod treated with 1500 ppm EA at 350 °C for 75 min. The concentration of DCE and EA is 275 ppm and 1500 ppm, respectively; GHSV: 15,000 h^{-1}; Catalysts: 200 mg.

is then replenished by molecular oxygen in the feed gas. The whole process involves alternative reduction and oxidation of the ceria surface with formation of oxygen vacancies and their successive replenishment by gas-phase oxygen. It can be seen that the oxygen vacancies play a key role in the catalysis oxidation of DCE and EA, the presence of oxygen vacancies facilitates the activation and transportation of active oxygen species. Furthermore, these vacancies expose exclusively Ce^{3+} ions, providing effective adsorption sites to gas phase DCE, and itself also is the adsorption sites of EA.

Scheme 1. The proposed reaction mechanism of catalytic combustion of DCE and EA over CeO_2 catalysts.

4. Conclusion

Single-crystalline and uniform CeO_2 nanorod, nanocube and nanoocta were selectively synthesized via an easy solution-based hydrothermal method. The as obtained CeO_2 nanocrystals showed different exposed crystal planes: (1 1 0) and (1 0 0) for nanorod, (1 0 0) for nanocube, and (1 1 1) for nanoocta. The characterization results indicated that CeO_2 nanorods are preferable in many kinds of physical and chemical properties, such as higher surface area, smaller crystallite size, more oxygen vacancies, higher OSC and higher mobility of oxygen. The catalysis oxidation of DCE and EA was investigated over these ceria exposed well-defined crystal planes. The results indicated that ceria nanorod showed the highest catalysis activities, followed by nanocube and nanoocta, showing a salient morphology dependent phenomenon that was mainly originated from the chemical properties of the exposed facets. Moreover, a possible reaction mechanism for the catalytic oxidation of DCE and EA over the ceria catalyst was proposed. Firstly, DCE and EA are absorbed and dissociated over different active sites, for DCE, Ce^{3+} is the main adsorption sites, EA absorb on oxygen vacancies, and then the activated DCE and EA are oxidized by lattice oxygen in the CeO_2. The partially reduced CeO_{2-x} is finally replenished by molecular oxygen in the feed gas.

Although CeO_2 was found to be a very active catalyst for the catalytic oxidation of CVOCs, its activity quickly diminished due to the strong adsorption of HCl or Cl_2 produced from the decomposition of CVOCs on CeO_2 surface and the block of active sites. We have found that if chlorine or chloride ions adsorbed on the CeO_2 surface can be removed or transferred enough rapidly, the activity of the catalyst could be maintained for long time. At present, we are trying to resolve the deactivation of CeO_2 by two ways: Ru supported and transition metal (such as Mn and V) doped CeO_2 nanocrystals exposed well-defined crystal plane (different morphology).
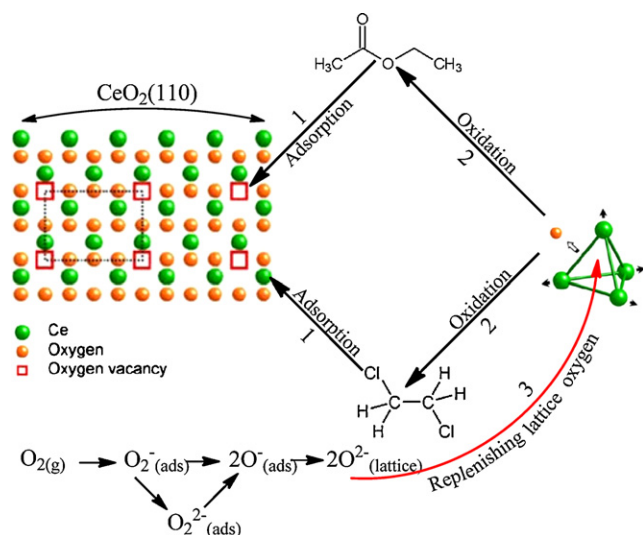
However, the formation of polychlorinated hydrocarbons by-products for Ru/CeO$_2$ catalysts, and the synthesis of transition metal doped CeO$_2$ binary oxide nanomaterials with tunable morphology is a troublesome problem.

Acknowledgments

Appendix A. Supplementary data

Supplementary data associated with this article can be found, in the online version, at doi:10.1016/j.apcatb.2012.02.001.

References

[1] Y. Dai, X.Y. Wang, Q.G. Dai, D. Li, Appl. Catal. B 111–112 (2012) 141–149.
[2] H.Y. Chang, S.P. Wang, J.R. Chang, H.S. Sheu, S.G. Shyu, Appl. Catal. B 111–112 (2012) 476–484.
[3] S. Pitkäaho, S. Ojala, T. Maunula, A. Savimäki, T. Kinnunen, R.L. Keiski, Appl. Catal. B 102 (2011) 395–403.
[4] H.F. Li, G.Z. Lu, Q.G. Dai, Y.Q. Wang, Appl. Catal. B 102 (2011) 475–483.
[5] B. de Rivas, R. López-Fonseca, M.Á. Gutiérrez-Ortiz, J.I. Gutiérrez-Ortiz, Appl. Catal. B 101 (2011) 317–325.
[6] B. de Rivas, R. López-Fonseca, M.A. Gutiérrez-Ortiz, J.I. Gutiérrez-Ortiz, Appl. Catal. B 104 (2011) 373–381.
[7] Y. Fan, X.B. Lu, Y.W. Ni, H.J. Zhang, M.W. Zhu, Y. Li, J.P. Chen, Appl. Catal. B 101 (2011) 606–612.
[8] C.E. Hetrick, F. Patcas, M.D. Amiridis, Appl. Catal. B 101 (2011) 622–628.
[9] Q.G. Dai, X.Y. Wang, G.Z. Lu, Appl. Catal. B 81 (2008) 192–202.
[10] Y. Dai, X.Y. Wang, D. Li, Q.G. Dai, J. Hazard. Mater. 188 (2011) 132–139.
[11] J.M. Zhou, L. Zhao, Q.Q. Huang, R.X. Zhou, X.K. Li, Catal. Lett. 127 (2009) 277–284.
[12] Q.Q. Huang, X.M. Xue, R.X. Zhou, J. Hazard. Mater. 183 (2010) 694–700.
[13] B. de Rivas, R. Lopez-Fonseca, C. Sampedro, J.I. Gutie rrez-Ortiz, Appl. Catal. B 90 (2009) 545–555.
[14] T. Mitsui, T. Matsui, R. Kikuchi, K. Eguchi, Top. Catal. 52 (2009) 464–469.
[15] P.O. Larsson, A. Andersson, J. Catal. 179 (1998) 72–89.
[16] S. Azalim, M. Franco, R. Brahmi, J.M. Giraudon, J.F. Lamonier, J. Hazard. Mater. 188 (2011) 422–427.
[17] M. Baudin, M. Wojcik, K. Hermansson, Surf. Sci. 468 (2000) 51–61.
[18] M. Nolan, S. Grigoleit, D.C. Sayle, S.C. Parker, G.W. Watson, Surf. Sci. 576 (2005) 217–229.
[19] M. Nolan, S.C. Parker, G.W. Watson, Surf. Sci. 595 (2005) 223–232.
[20] M. Nolan, J.E. Fearon, G.W. Watson, Solid State Ionics 177 (2006) 3069–3074.
[21] M. Nolan, G.W. Watson, J. Phys. Chem. B 110 (2006) 16600–16606.
[22] K.B. Zhou, X. Wang, X.M. Sun, Q. Peng, Y.D. Li, J. Catal. 229 (2005) 206–212.
[23] H.X. Mai, L.D. Sun, Y.W. Zhang, J. Phys. Chem. B 109 (2005) 24380–24385.
[24] W.I. Hsiao, Y.S. Lin, Y.C. Chen, C.S. Lee, Chem. Phys. Lett. 441 (2007) 294–299.
[25] R. Si, F.S. Maria, Angew. Chem. Int. Ed. 47 (2008) 2884–2887.
[26] Tana, M.L. Zhang, J. Li, H.J. Li, Y. Li, W.J. Shen, Catal. Today 148 (2009) 179–183.
[27] X.W. Liu, K.B. Zhou, L. Wang, B.Y. Wang, Y.D. Li, J. Am. Chem. Soc. 131 (2009) 3140–3141.
[28] W.T. Chen, K.B. Chen, M.F. Wang, S.F. Weng, C.S. Lee, M.C. Lin, Chem. Commun. 46 (2010) 3286–3288.
[29] H.J. Li, G.S. Qi, Tana, X.J. Zhang, W. Li, W.J. Shen, Catal. Sci. Technol. 1 (2011) 1677–1682.
[30] L. Yan, R.B. Yu, J. Chen, X.R. Xing, Cryst. Growth Des. 8 (2008) 1474–1477.
[31] V.G. Keramidas, W.B. White, J. Chem. Phys. 59 (1973) 1561–1563.
[32] W.H. Weber, K.C. Hass, J.R. McBride, Phys. Rev. B 48 (1993) 178–185.
[33] M. Swanson, V.V. Pushkarev, V.I. Kovalchuk, J.L. D'Itri, Catal. Lett. 116 (2007) 41–45.
[34] J.R. McBride, K.C. Hass, B.D. Poindexter, W.H. Weber, J. Appl. Phys. 76 (1994) 2435–2462.
[35] Z. Wu, M. Li, J. Howe, H.M. Meyer, Langmuir 26 (2010) 16595–16606.
[36] Z.V. Popovic, Z. Dohcevic-Mitrovic, A. Cantarero, J. Phys.: Condens. Matter 19 (2007) 496209–496238.
[37] Z.V. Popovic, Z. Dohcevic-Mitrovic, M.J. Konstantinovic, M. Scepanovic, J. Raman Spectrosc. 38 (2007) 750–755.
[38] J.C. Conesa, Surf. Sci. 339 (1995) 337–352.
[39] R. Di Monte, J. Kaspar, Top. Catal. 28 (2004) 47–57.
[40] J. Zhang, H. Kumagai, K. Yamamura, Nano Lett. 11 (2011) 361–364.
[41] Z. Yang, T.K. Woo, M. Baudin, K. Hermansson, J. Chem. Phys. 120 (2004) 7741–7750.
[42] T.X.T. Sayle, S.C. Parker, C.R.A. Catlow, Surf. Sci. 316 (1994) 329–336.
[43] N.V. Skorodumova, M. Baudin, K. Hermansson, Phys. Rev. B 69 (2004) 75401–75409.
[44] M. Nolan, S. Grigoleit, D.C. Sayle, Surf. Sci. 576 (2005) 217–229.
[45] C. Pan, D. Zhang, L. Shi, J. Fang, Eur. J. Inorg. Chem. 15 (2008) 2429–2436.
[46] B. Ramachandran, H.L. Greene, S. Chatterjee, Appl. Catal. B 8 (1996) 157–182.
[47] H. Norenberg, J.H. Harding, Surf. Sci. 477 (2001) 17–24.
[48] J. Soria, J.C. Conesa, A. Martinez-Arias, Colloids Surf. A 158 (1999) 67–74.
[49] C.R.A. Catlow, J. Chem. Soc. Faraday Trans. 86 (1990) 1167–1176.